INORGANIC CHEMISTRY
FRONTIERS

RESEARCH ARTICLE

View Article Online
View Journal | View Issue

Cite this: *Inorg. Chem. Front.*, 2024, **11**, 8037

Mesoscopic spiral nanoplates formed by porphyrin-spaced coordination frameworks for enhanced H_2O_2 photosynthesis†

Liang He, [a] Er-Xia Chen,[a,b] Ju-Qiang Xiang,[a,d] Yu-Jun Guo,[a] Jian Zhang *[a] and Qipu Lin *[a,c]

Although tremendous efforts have been devoted to regulating the morphology of metal–organic frameworks (MOFs), it is still a substantial challenge to achieve chirality at the crystal morphological level. This work presents a bottom-up synthetic approach to produce chiral morphological bismuth-based porphyrin MOFs, featuring a unique surface morphology – a square spiral terrace-shaped crystal that exhibits mesoscopic mirror-symmetry breaking. Compared with bulk samples, screw dislocation defects could promote the anisotropic growth of the square spiral terrace-shaped nanoplates under conditions of low supersaturation concentrations and in the presence of polyvinyl pyrrolidone (PVP). To assess the effect of the anisotropic morphology on the properties, photocatalytic hydrogen peroxide (H_2O_2) production experiments under pure water and oxygen conditions (blue LED illumination, λ = 455 nm) were carried out. The experimental results showed that the screw dislocation nanoplates displayed 1.5 times higher photocatalytic activity (156.22 μM h^{-1}) than that of bulk samples (106.24 μM h^{-1}). This may be attributed to the better dispersion in water and fully exposed catalytically active sites of the screw dislocation nanoplates. These findings provide novel insights for obtaining MOFs with a chiral morphology and improving the photocatalytic H_2O_2 generation based on morphological control.

Received 25th June 2024,
Accepted 30th September 2024

DOI: 10.1039/d4qi01580k

rsc.li/frontiers-inorganic

Introduction

Supramolecular chirality plays a pivotal role in diverse fields such as optoelectronics,[1] biology,[2] asymmetric catalysis,[3] and materials science.[4] The self-assembly of achiral molecules into supramolecular structures can lead to racemates or homochiral domains, involving symmetry breaking – a key factor in the genesis of homochirality.[5] Among them, porphyrin-based systems have attracted significant attention because they could induce chiral organization by electrostatic, hydrogen-bonding and dispersive interactions.[6] For instance, despite the lack of inherent chirality in tetraphenyl sulfonate porphyrin, helical aggregates are formed by tetraphenyl sulfonate porphyrins because of rotational and magnetic forces.[7] However, most studies on controlling chiral self-assembly with porphyrins have focused on amorphous materials, which poses challenges in elucidating molecular level processes.[8] Crystalline multi-porphyrin architectures offer well-ordered structures, enabling precise definition of the spatial arrangements and distances between porphyrin units.[9] Metal–organic frameworks (MOFs), a significant type of crystalline porous materials, present an excellent platform for investigating chiral aggregation processes. Constructing chiral MOFs (C-MOFs) from achiral porphyrin precursors allows for a better understanding of the mechanisms governing chiral self-assembly.[10]

Extensive efforts have been made to develop MOFs' structures and investigate their properties in the past few decades. However, researchers increasingly focus on the macroscopic characteristics of MOFs in recent years, especially their crystal sizes, shapes, and morphologies.[11] For instance, two-dimensional (2D) metal–organic nanosheets (MONs) have garnered significant interest due to their enhanced catalytic properties. Compared to three-dimensional (3D) bulk MOFs, MONs are capable of exposing more active sites and reducing the path of electron transport in the reaction, thereby facilitating the cata-

[a]*State Key Laboratory of Structural Chemistry, Fujian Institute of Research on the Structure of Matter, Chinese Academy of Sciences, Fuzhou, Fujian 350002, China. E-mail: zhj@fjirsm.ac.cn, linqipu@fjirsm.ac.cn*
[b]*Fujian Science & Technology Innovation Laboratory for Optoelectronic Information of China, Fuzhou, Fujian 350108, China*
[c]*State Key Laboratory of Photocatalysis on Energy and Environment, Fuzhou University, Fuzhou, 350116, China*
[d]*College of Chemistry and Materials Science, Fujian Normal University, Fuzhou, Fujian 350117, China*

†Electronic supplementary information (ESI) available: Detailed experimental procedures, X-ray crystallographic data and additional characterization figures. CCDC 2294422. For ESI and crystallographic data in CIF or other electronic format see DOI: https://doi.org/10.1039/d4qi01580k

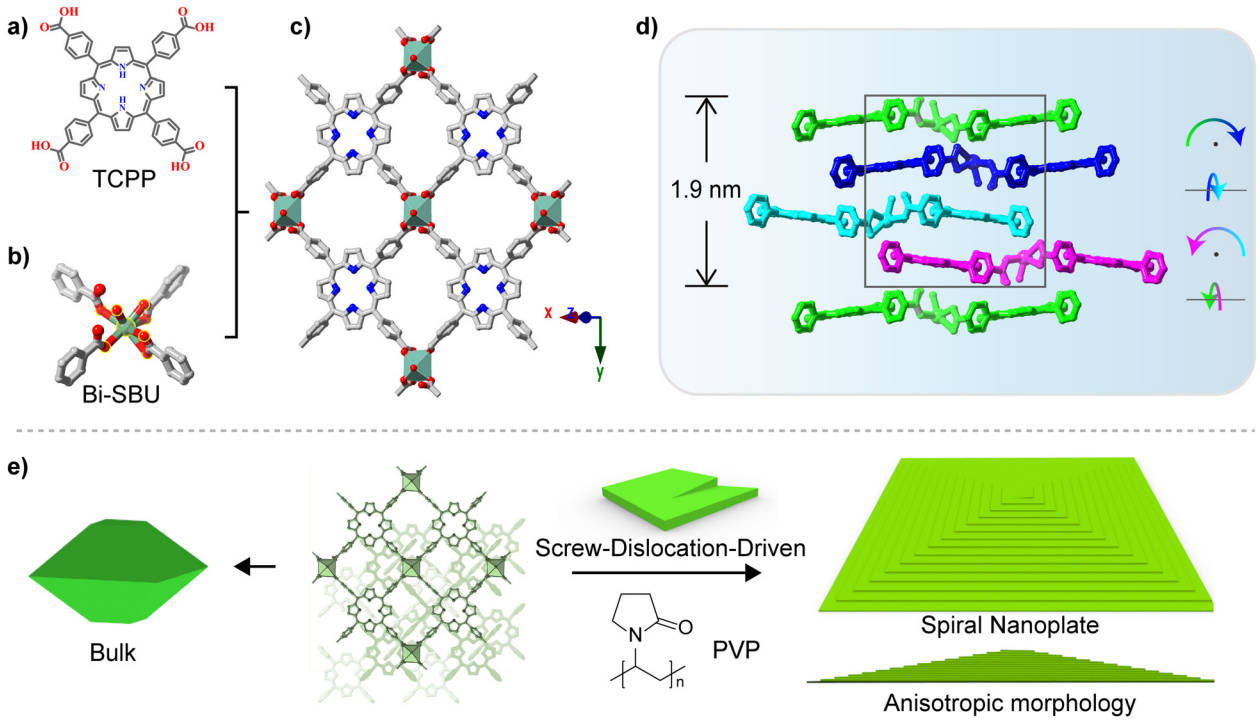

Fig. 1 (a–c) Structure of Bi-TCPP and its assembly units, *viz*. Bi-carboxylate node and TCPP linker. (d) Side-view of the stacking mode of 2D layers in Bi-TCPP along the *b*-axis. (e) Diagram of growth mechanism for Bi-TCPP-bulk and Bi-TCPP-NPs.

lytic process.[12] For synthetic chemists, obtaining MONs with uniform and large sizes presents a significant challenge. While extraction of MONs from layered 2D MOFs *via* ultrasonic stripping offers a straightforward strategy, controlling exfoliation often yields nonuniform size and thickness. An alternative approach involves direct bottom-up synthesis, which is preferable for fabricating MONs with high yield, controllable thickness, and large lateral dimensions. However, predicting and designing crystal morphology remains challenging due to the myriad of influencing parameters, *e.g.*, temperature, solvent, and additives used during crystal growth. Modulators have been proved to be effective in manipulating the crystal morphology, even in complex chiral architectures.[13] The controlled growth of crystalline surfaces using modulators has also been employed to tailor crystal facets of MOFs. Some achiral MOFs deviate from long-range translational order by twisting and bending during growth on another crystal surface, resulting in crystals exhibiting square spiral terrace-shaped facets.[14] Nevertheless, these helical dislocations do not conform to a separate single crystal model. Moreover, these structures are derived from 3D MOF architectures, and the realization of this helical morphology in 2D MOFs has not yet been documented. However, there are some studies by van der Boom M. E. *et al.* on the construction of chiral pyridine-based MOFs at both molecular and macroscopic scales.[15] Nevertheless, the pathway for forming crystals with chiral morphology is still poorly understood and the exploration of their related performance is insufficient.

Bismuth ions (Bi^{3+}) are recognized for their high coordination numbers and flexible coordination environments. As a result, metal complexes containing Bi^{3+} often adopt a twisted conformation. Moreover, Bi^{3+} and its complexes are known for their non-toxicity, making them appealing for environmentally friendly catalysts and medical applications.[16] However, research on Bi^{3+}-containing MOFs has been limited.[17] Herein, we successfully synthesized bismuth-based C-MOFs, denoted as Bi-TCPP, featuring 2D layers and utilizing the achiral ligand tetrakis(4-carboxylphenyl) porphyrin (TCPP).[18] The crystal growth process was controlled using a modulator-assisted synthetic method, resulting in a unique square spiral terrace morphology (Fig. 1). Furthermore, we evaluated its photocatalytic activity for H_2O_2 production under 455 nm LED irradiation, demonstrating excellent performance in pure water without any sacrificial agent.

Results and discussion

The single-crystal X-ray diffraction (SC-XRD) analysis reveals that Bi-TCPP crystallizes in the chiral space group $P2_12_12_1$. As shown in Fig. 1a–c, each unit of Bi-TCPP features a Bi^{3+} site with a 4-connected coordination configuration, formed by four carboxyl groups from TCPP ligands nearly positioned in the same *ab* plane. Consequently, a 2D layered network with a (4,4)-connection *sql* topology is constructed. Additionally, a water molecule coordinates with Bi^{3+} along the *c*-axis, establishing hydrogen bonds with carboxylate oxygens. The chirality of Bi-TCPP arises from the non-centrosymmetric porphyrin unit, which is axially polarized, and the distorted tetrahedral

Bi^{3+} node, leading to the formation of 'wavy' bismuth–porphyrin layers (Fig. 1d). Neighboring layers relate to each other through crystallographic symmetry manipulation. Stacking of these corrugated sheets occurs uniformly in an ABCD mode, supported by crystallographic translation. The average distance between overlapping porphyrin rings is 6.3 Å, as depicted in Fig. S2.† Such stacking fashion is remarkably rare, indicating a unique coexistence of rotary multilayers within a single crystal. The layer stacking gives rise to 1D nanosized spiral channels with a cross-section of approximately 4×4 $Å^2$ along the *c*-axis. PLATON analysis demonstrates that the structure contains large solvent-accessible voids, calculated to be 5633.9 $Å^3$, constituting 40.8% of the unit cell volume. Although the diffraction-based structural model of Bi-TCPP clearly displays a chiral architecture, crystallographic refinement indicates the presence of inversion twins, signifying the co-crystallization of different enantiomeric components.

Most bulk crystals possess a well-organized, symmetrical shape. The scanning electron microscopy (SEM) image in Fig. 2a illustrates the inherent layered structure of Bi-TCPP. It is worth noting that spiral growth morphologies are also observed in some bulk samples (Bi-TCPP-bulk, Fig. 2b and Fig. S3–S6 in the ESI†), which prompts further investigation into the influence of screw dislocations on growth kinetics along different crystallographic directions and assesses the impact of strain energy on the equilibrium shapes of defective crystals. For this purpose, we carried out the experiments by adding a modulator (polyvinyl pyrrolidone, PVP) into the growth solution with a low reactant concentration (see the ESI†). Morphological examination of intermediate products during the reaction process (see the ESI†) revealed the formation of a unique material with a square spiral terrace characteristic (Bi-TCPP-NPs) at the initial 4 hour stage, as detected *via* SEM (Fig. S7 in the ESI†). This morphology can be described as a set of spiral open-loops gradually rotating along the 001 axis, with terraces aligned parallel to the ⟨100⟩ direction. Notably, SEM images show that spirals appear on one side of a nanoplate, while the other side remains smooth. AFM measurements revealed a thickness of *ca.* 200 nm for the nanoplates at the 4 hour stage (Fig. S8a in the ESI†). Additionally, a flower-like structure composed of

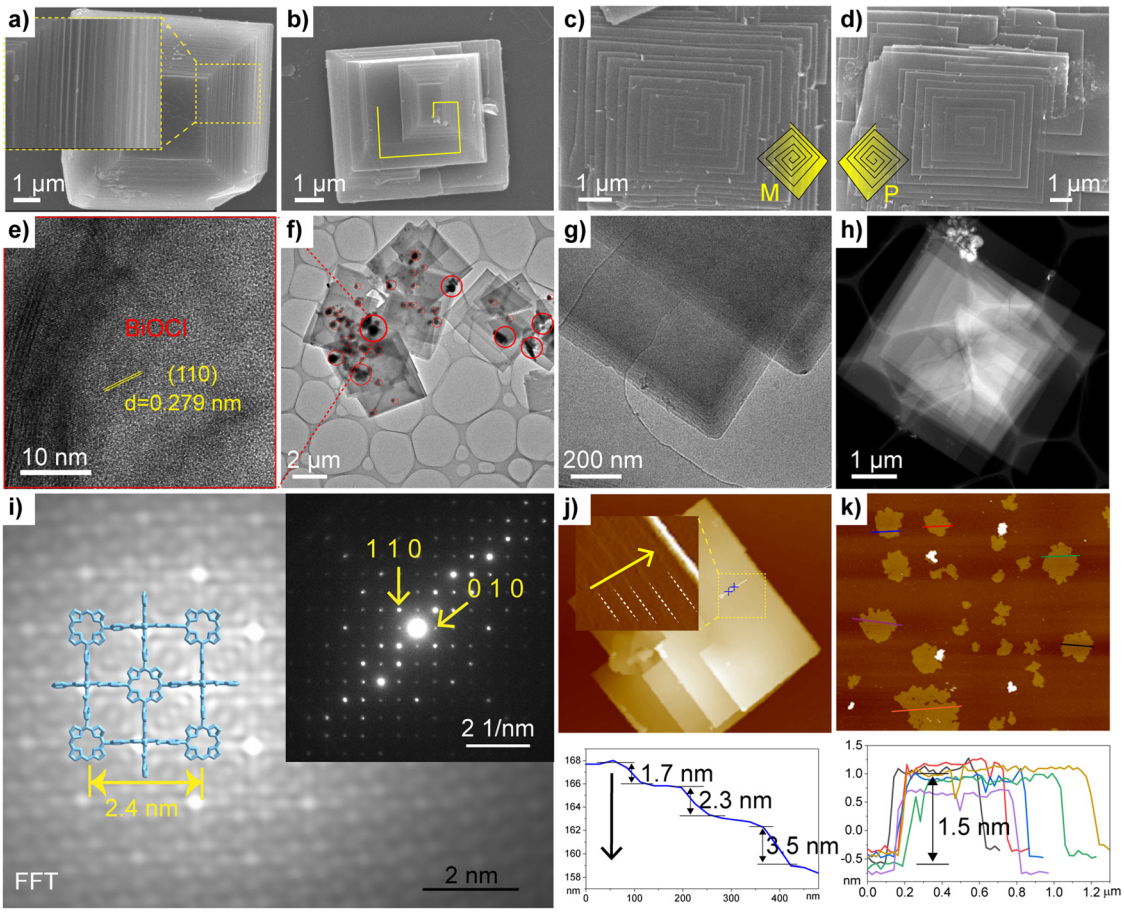

Fig. 2 Morphologies of normal growth (a) and spiral growth (b) in bulk crystals of Bi-TCPP. (c and d) SEM images of Bi-TCPP nanoplates with left-handed (M) and righthanded (P) configurations. (e–h) TEM images of different scales of Bi-TCPP nanoplates, accompanied by cocrystallite BiOCl circled in red at the beginning of the reaction. (i) HAADF image and FFT pattern of the nanoplates of Bi-TCPP. (j) AFM image of the nanoplates of Bi-TCPP *via* cross-sectional analysis of its growth steps on the helical surfaces. (k) AFM image of the nanosheets of Bi-TCPP after exfoliation and their height profiles.

numerous interleaving nanosheet petals was noticed. Extending the reaction time to 8 hours resulted in more prominent nanoplates with larger terraces, reaching a mesoscopic diameter of *ca.* 10 μm. During this stage, we also noted a significant increase in edge site growth. Subsequent crystal growth over approximately 24 hours resulted in nanoplate thickening to the micron level (Fig. S8b in the ESI†). The emergence of spiral nanoplate morphology can be explained through the Burton–Cabrera–Frank (BCF) theory.[19] When a screw dislocation intersects a crystal surface, it generates step edges that propagate as self-sustaining growth spirals. Under conditions of low supersaturation, if the velocity of steps at the dislocation core (v_c) matches that at the outer edges (v_o), the resulting dislocation hillocks exhibit a shallow slope, forming highly flattened pyramids resembling nanoplates. In addition, as the nanoplates grew, the flower-like material gradually diminished and eventually disappeared. To validate these observations, we monitored the reaction using powder XRD (PXRD) to study the phase transition (Fig. S9 in the ESI†). The nanoplates were identified as Bi-TCPP, and their conversion from the flower-like phase was consistent with the PXRD data. Furthermore, we obtained a pure phase of the flower-like material by adjusting conditions without the TCPP ligand. This compound was further characterized using elemental analysis, PXRD, SEM and transmission electron microscopy (TEM) (Fig. S10–S12 in the ESI†). All results confirmed the flower-like material as BiOCl. The above findings collectively indicate a transition process from BiOCl to Bi-TCPP-NPs.

Fig. 2c and d depict two spirals with opposite directions creating open-loop terraces. These spirals are commonly referred to as left-handed (M) and right-handed (P) configurations according to conventional nomenclature. This observation suggests symmetry breaking at the morphological level within a porphyrinic MOF system. However, it is quite difficult to determine the orientation of the helical configuration and accurately quantify the populations of both forms due to the presence of various other twisted shapes. Thus, it can be inferred that there is a relative rather than absolute symmetry breaking in this system. The primary objective of our study was to explore spiral morphology using atomic force microscopy (AFM) to examine the crystal layer surface. Our observations indicated numerous minor steps on the leading spiral surface (Fig. 2j). On the opposite side of the crystal, we observed square-growth hillocks resembling stacks of islands formed from spiral loops (Fig. S13 in the ESI†). The height of these minor steps is approximately 2 nm, which is comparable to the d_{001} crystal spacing (1.9 nm), which corresponds to the height of a four-layer bismuth–porphyrin array along the *c*-axis. The crystal surface is commonly regarded as either "spiral growth" or "screw dislocation", typical topological defects that arise during crystal growth. The major steps, which are 50 nm in height, consist of numerous layers of minor steps, thereby generating spiral nanosheets (Fig. S8 in the ESI†).

The square terraces were further analyzed using TEM and selected area electron diffraction (SAED). Dark-field TEM images revealed the rotational growth of layers that shared a screw axis (Fig. 2h), while single-crystal SAED patterns were detected under the high-energy electron beam of TEM (Fig. 2i). Additionally, the fast Fourier transform (FFT) patterns of the nanoplates exhibited a distinct porphyrin plane with a four-connection *sql* topology distribution, closely matching the {001} facets. The inverse FFT image of the diffraction point in Fig. S14† shows lattice displacement of the line defect (marked with a red line), characteristic of screw dislocation. Notably, the stacked flake spiral morphology enabled the production of micron-sized and ultrathin nanosheets through solvent-assisted liquid sonication. Examination of terrace height indicated a thickness of approximately 1.5 nm (Fig. 2k). Various dislocations exist in nature, but the square spiral terrace shape has only been seen in a few achiral MOFs. Isochiral screw dislocations have been proposed as a potential cause for "Eshelby twisting", a well-established origin of chirality.[13,20] On one hand, the introduction of PVP can disrupt crystal growth symmetry, promoting growth driven by dislocations under conditions of low supersaturation. On the other hand, chiral-like stacking with frustrated packing, which refers to layer discontinuity, tends to produce a helical morphology. Our findings emphasize the presence of macroscopic spiral morphologies in complex MOFs characterized by both chirality and the 2D architecture.

The regulation of morphology notably affects optical signals, as illustrated in Fig. S15,† where the circular dichroism (CD) spectrum of Bi-TCPP nanoplates displays signals corresponding to the porphyrin absorption. In contrast, the CD spectra of bulk Bi-TCPP samples exhibit negative Cotton effects (CE) around 415 nm and 440 nm (Fig. S16 in the ESI†). The characteristic Soret band is distinctly visible for nanoplate samples, accompanied by negative shoulder CEs at *ca.* 395 nm, 433 nm, 447 nm and 477 nm. Moreover, enhanced CD signals between 450 and 700 nm indicate amplification of the Q band signal in nanoplate samples. Remarkably, consistent CD curves of nanoplate samples prepared from different batches were obtained (specifically, the CD spectra were obtained from 30 collections). Generally, when achiral molecules self-aggregate, they form structures that are either achiral or racemic, lacking CD signals. However, the contribution of linear dichroism (LD) to CD signals must be considered. The LD spectra of nanoplates exhibit mirror-imaged curves compared to their CD, with strong absorption of *ca.* 2×10^{-2}. The LD artifact contributes an estimated 60% to the CD signal, underscoring the substantial role of system anisotropy in the measured CD.[21] Inversely, LD spectra of bulk samples show profiles distinct from their corresponding CD spectra, with optical densities below 1×10^{-3}, contributing negligibly to the overall CD spectra. Accordingly, the CD signal likely originates from the macroscopic anisotropic alignment of nanoplates, which exhibit significant linear optical polarization along their screw axis, rather than intrinsic chirality. This anisotropic optical crystal holds the potential for applications in polarized fluorescence, photocurrent generation, and other areas (Fig. S17 in the ESI†).

The N_2 adsorption–desorption isotherm of Bi-TCPP at 77 K showed no uptake (Fig. S18 in the ESI†), which ascribes to its

ultra-microporosity that restricts the entry of N_2 molecules due to their relatively large dynamic diameter. The permanent porosity of Bi-TCPP was confirmed by CO_2 adsorption–desorption at 195 K and the Brunauer–Emmett–Teller (BET) surface area is 492.31 $m^2\ g^{-1}$. The CO_2 isotherms displayed type-I behavior, indicating the microporous nature of Bi-TCPP. Water vapor adsorption tests revealed hydrophilic pores in the sample (9.96 mmol g^{-1}, 95% relative humidity), which enhances its suitability for subsequent photocatalysis in water by facilitating water adsorption and sample dispersion (Fig. S19 in the ESI†). Thermal gravimetric (TG) analysis and temperature-dependent PXRD were conducted to explore the thermal stability of Bi-TCPP. Coordinated water was readily removed at a temperature of *ca.* 160 °C, while framework decomposition initiated at approximately 300 °C (Fig. S20 and S21 in the ESI†). Compared to other chiral MOFs, the incorporation of Bi-O connectors into Bi-TCPP resulted in a robust, chiral framework capable of retaining porosity even after activation. Furthermore, no significant loss of crystallinity was observed for Bi-TCPP after 24 hour exposure to water and various solvents (Fig. S22 in the ESI†), confirming its outstanding chemical stability.

Ultraviolet–visible–near infrared diffuse reflection spectra (UV-vis-NIR DRS) demonstrate that Bi-TCPP-NPs exhibit a broad optical absorption range, with absorption edges near 1000 nm, suggesting excellent light-harvesting ability in the visible and near-infrared regions (Fig. 3a). The band gap (E_g) of Bi-TCPP-NPs was calculated to be 1.78 eV using the Kubelka–Munk function (Fig. 3b). UV-vis-NIR absorption spectra of TCPP, TCPP-bulk and BiOCl are provided for comparison. TCPP and Bi-TCPP-bulk show absorption profiles similar to that of Bi-TCPP-NPs, whereas BiOCl absorbs only at 400 nm (Fig. S23 in the ESI†). The narrow E_g of Bi-TCPP-NPs, enabling efficient photon capture, suggests that these supramolecular photocatalysts may enhance photocatalytic activity for H_2O_2 production under visible light. Mott Schottky measurements (Fig. 3c) were performed to further study the electronic structures. The positive slope of the fitted line indicates that Bi-TCPP-NPs are n-type semiconductors, with flat band potentials (E_{FB}) of Bi-TCPP-NPs determined as −0.51 V (*vs.* NHE, pH = 7). The valence band potential (E_{VB}) was calculated according to the equation $E_{VB} = E_g + E_{CB}$, yielding a value of 1.25 V. The E_{CB} of Bi-TCPP-NPs exceeds the reduction potential of O_2/H_2O_2 (0.68 V *vs.* NHE, pH = 7), indicating that

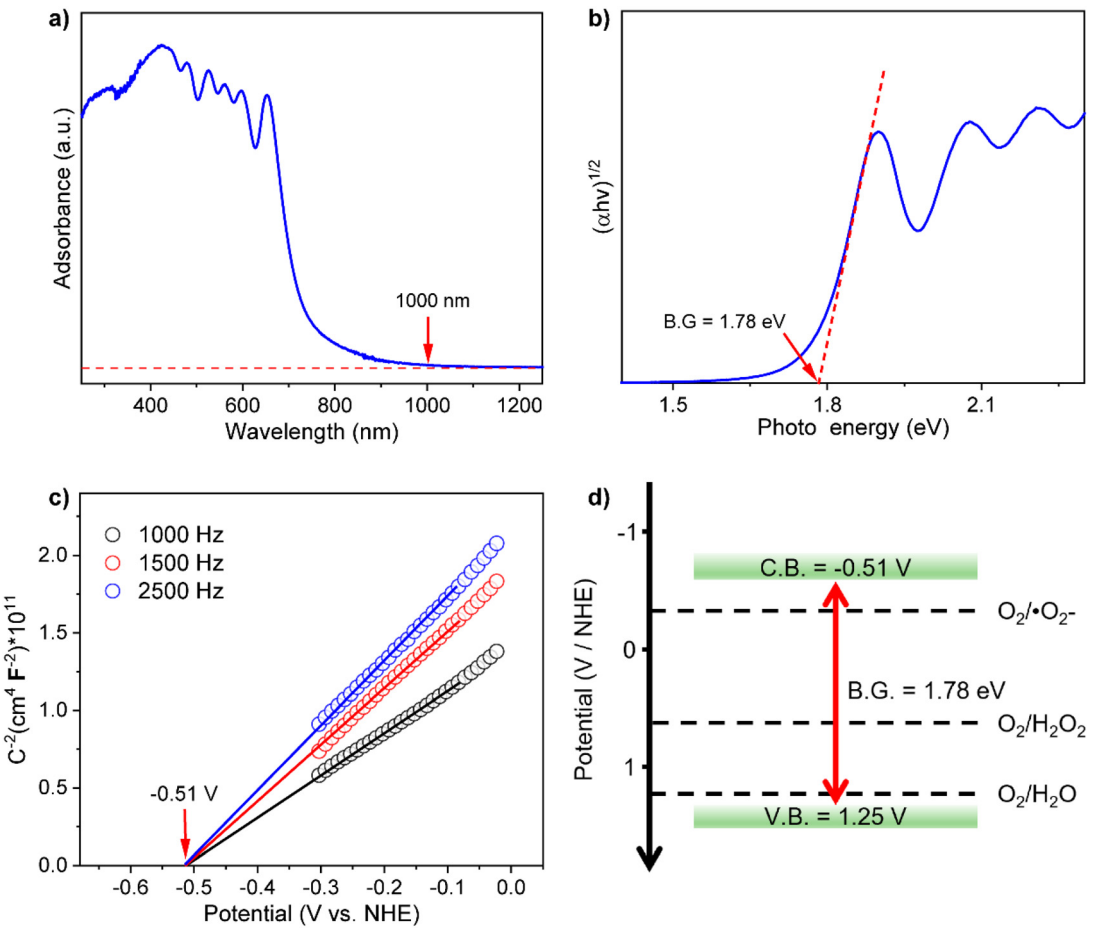

Fig. 3 (a) UV-vis-NIR DRS of Bi-TCPP-NPs. (b) Tauc plot for band-gap calculation of Bi-TCPP-NPs. (c) Mott–Schottky plots of Bi-TCPP-NPs. (d) Band structure diagram of Bi-TCPP-NPs.

Bi-TCPP-NPs facilitate the transfer of photogenerated electrons on their surface for the conversion of O_2 to H_2O_2. The E_{VB} of Bi-TCPP-NPs is more negative than the oxidation potential of H_2O/H_2O_2 (1.78 V *vs.* NHE, pH = 7), implying that direct transfer of photogenerated holes to H_2O_2 is hindered. Conversely, water oxidation to O_2 may occur due to the redox potentials (1.23 V *vs.* NHE, pH = 7) being lower than the E_{VB}. The band structures indicate that Bi-TCPP-NPs are thermodynamically suitable for the overall photocatalytic H_2O_2 production under pure water and oxygen conditions (Fig. 3b).

Bi-TCPP-NPs exhibit narrow band gaps, appropriate electronic structures, high water stability, and hydrophilicity, all of which are highly favorable for investigating their photocatalytic activity in water. Importantly, nanoplates with helical dislocation morphology have thinner dimensions compared to bulk samples, which facilitates their dispersion in water (Fig. S24†). Bi-TCPP-NPs also exhibit an enhanced photocurrent response and impedance, which conduces to the efficient transport of photogenerated charge carriers and separation of electron–hole pairs under visible-light irradiation (455 nm LED, Fig. S25 and S26†). Moreover, the presence of mesoscopic scales and dislocation defects ensures effective exposure of catalytic sites in 2D materials. Taking these factors into account, we examined the photocatalytic capabilities of BiOCl, TCPP, TCPP-bulk and TCPP-NP samples under visible light irradiation. Photocatalytic H_2O_2 production activities were conducted in O_2-saturated pure water under blue LED light (λ = 455 nm, 0.2 W cm^{-2}), without additional reagents such as sacrificial agents, photosensitizers or pH adjustment. These catalysts (15 mg) were dispersed in 30 mL of pure water, respectively, and the concentration of generated H_2O_2 was measured after one hour. Bi-TCPP-NPs exhibited the highest H_2O_2 concentration at 156.22 μM, contrasting with 106.24 μM for Bi-TCPP-bulk, 23.97 μM for TCPP, and a minimal H_2O_2 yield for BiOCl (Fig. 4a). The superior catalytic activity of Bi-TCPP-NPs is attributed to their hydrophilic pores, better dispersion and sufficient exposure of catalytically active sites. The reduced catalytic activity of TCPP and BiOCl may stem from their weak responsiveness to visible light and inherent structural characteristics. While nanosheets obtained by mechanical exfoliation of the

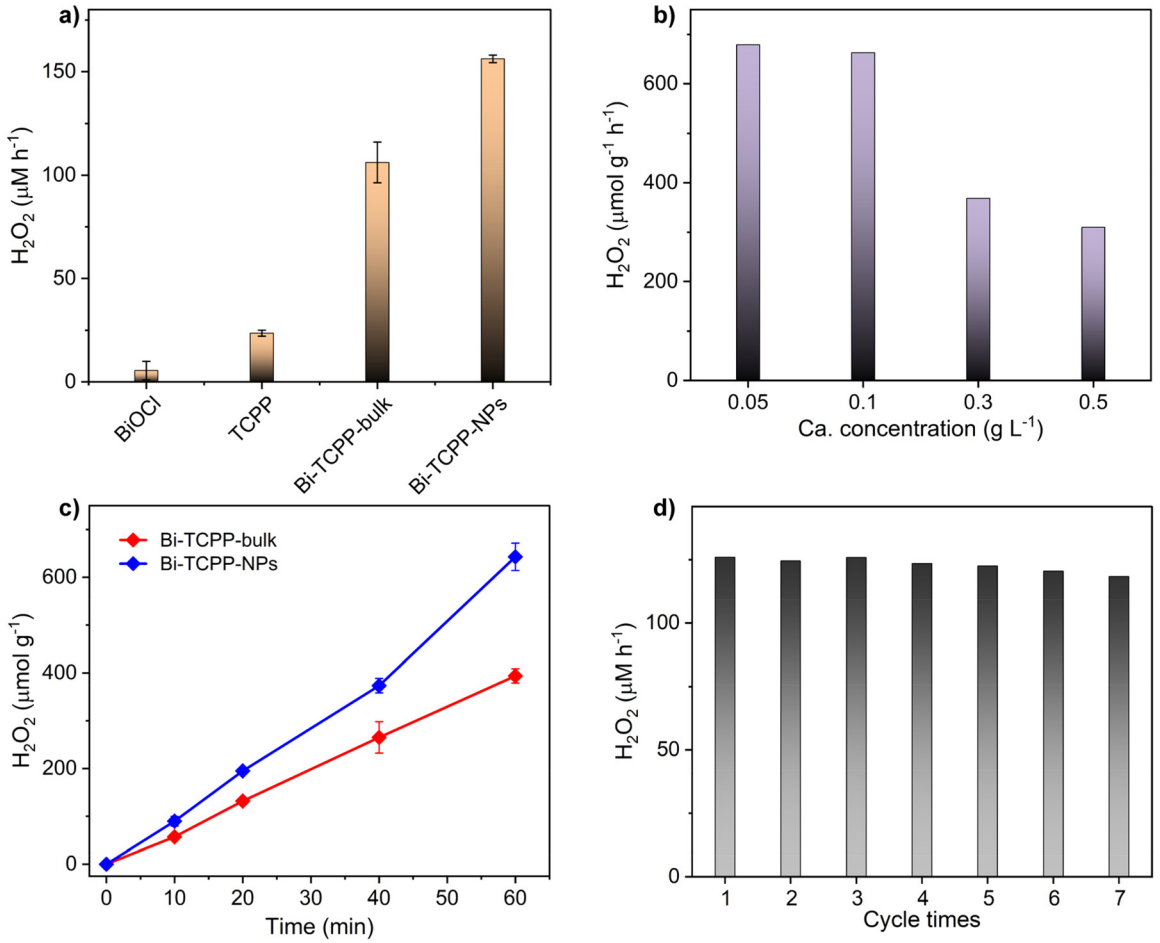

Fig. 4 (a) Time-dependent photocatalytic H_2O_2 production for BiOCl, TCPP, Bi-TCPP-bulk and Bi-TCPP-NPs (15 mg of catalyst in 30 mL of water under visible light, LED 455 nm, for 1 hour). (b) H_2O_2 production of Bi-TCPP-NPs at different catalyst amounts (30 mL of water under LED 455 nm for 1 hour). (c) H_2O_2 production on Bi-TCPP-NPs and Bi-TCPP bulk (0.1 g L^{-1}, 30 mL of water under LED 455 nm). (d) Cyclic stability for H_2O_2 production of Bi-TCPP-NPs (0.5 g L^{-1}, 30 mL of water under LED 455 nm).

TCPP-NP samples also undergo the photocatalytic reaction, their small size complicates the separation of liquid phase products and catalysts, precluding product detection (Fig. S28 in the ESI†). Increasing the amounts of Bi-TCPP-NPs enhances activity, though H_2O_2 production rates exhibit a decreasing trend. The optimal production rate of 679.79 μmol g^{-1} h^{-1} is achieved at a catalyst concentration of 0.05 g L^{-1} (Fig. 4b and Fig. S29 in the ESI†). Compared with photocatalysts that do not use sacrificial reagents, the catalytic efficiency of Bi-TCPP-NPs is very close to that of state-of-the-art MOFs (Table S2†).[22] Moreover, Bi-TCPP-NPs significantly outperform bismuth-based MOFs synthesized with non-porphyrin ligands, as well as extensively investigated C_3N_4-based materials.[23] However, their performance is lower than that of some recently emerged covalent organic frameworks (COFs).[24] Fig. 4c shows a steady increase in H_2O_2 production in an hour irradiation period for Bi-TCPP-NPs and Bi-TCPP-bulk. Cycling experiments reveal that Bi-TCPP-NPs can be effectively recovered by centrifugation and reused with negligible degradation in performance. Activity declines after seven cycles, which indicates the high durability of Bi-TCPP-NPs (Fig. 4d). Meanwhile, ICP, TEM, XPS, PXRD and FTIR analyses demonstrate that the structure and morphology of Bi-TCPP-NPs remained unchanged after photocatalysis, underscoring their excellent stability in H_2O_2 synthesis (Table S3 and Fig. S30–S34 in the ESI†).

Considering that oxygen reduction reactions (ORRs) and water oxidation reactions (WORs) are two potential pathways involved in the photosynthesis of H_2O_2, we conducted control experiments to unveil its generation during photocatalysis. As shown in Fig. 5a, under a O_2 atmosphere, H_2O_2 production reached 157.53 μM, whereas with air, it decreased to 72.55 μM. Trace amounts of H_2O_2 were detected under an Ar atomosphere. Negligible H_2O_2 formed in the dark. In the presence of $AgNO_3$ (electron-trapping agent), minimal H_2O_2 was generated. Trapping holes with CH_3OH (142.14 μM) reduced H_2O_2 generation slightly, indicating holes are not directly involved in photocatalytic H_2O_2 production. These results suggest that photo-generated electrons reducing O_2 is the main pathway for H_2O_2 production. Addition of *p*-benzoquinone (*p*-BQ, superoxide radical scavenger, $^{\bullet}O_2^-$) drastically decreased H_2O_2 production (24.89 μM), suggesting H_2O_2 formation *via* the sequential two-step single electron ORR pathway ($O_2 + e^- \rightarrow {}^{\bullet}O_2^-$, ${}^{\bullet}O_2^- + 2H^+ + e^- \rightarrow H_2O_2$). Electron paramagnetic spectroscopy (EPR) using 5,5-dimethyl-1-pyrroline *N*-oxide (DMPO) as a radical trapping

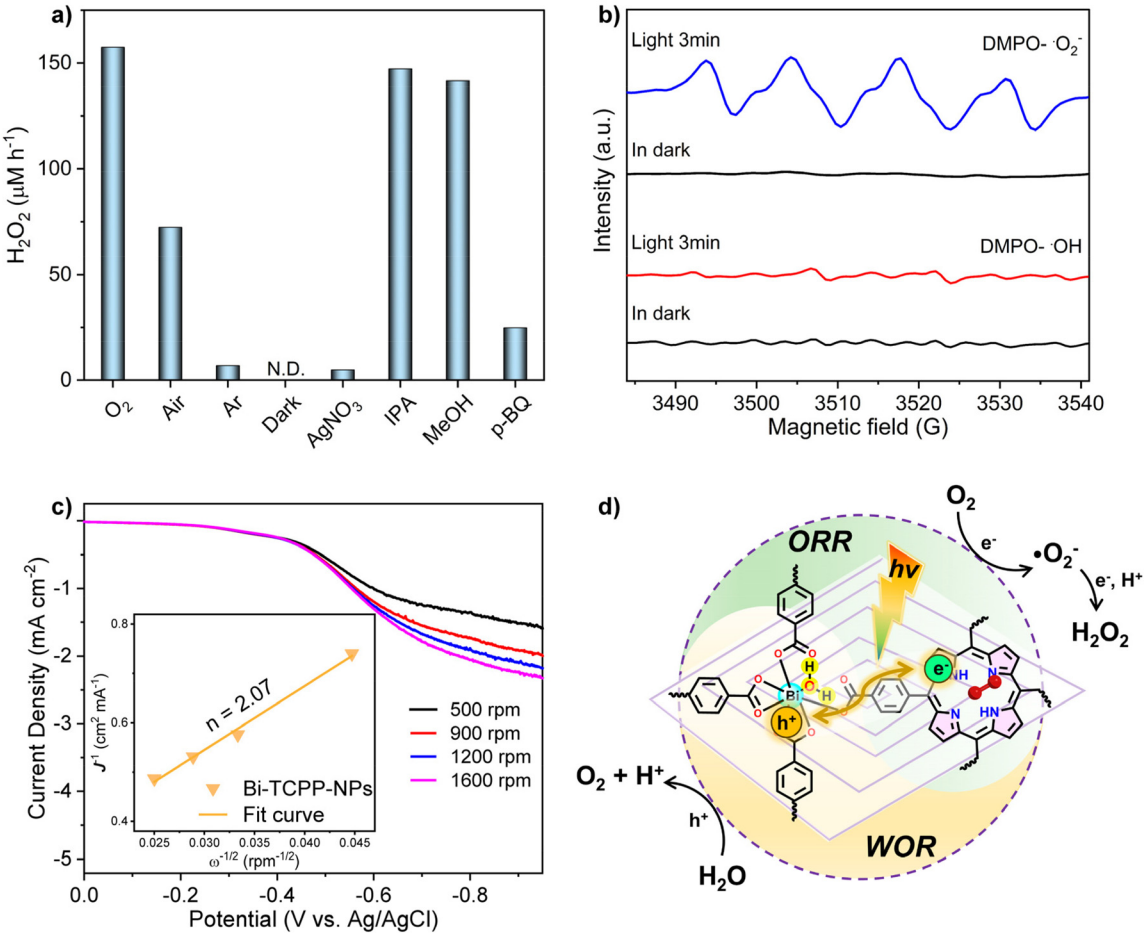

Fig. 5 (a) The photocatalytic H_2O_2 production rates with different scavengers and atmospheres. (b) EPR spectra of Bi-TCPP-NPs. (c) The Koutecky–Levich plots obtained by RDE measurements at −0.80 V *vs.* Ag/AgCl. (d) The proposed mechanistic catalytic diagrams over Bi-TCPP-NPs.

agent identified DMPO-$^{\bullet}O_2^-$ signals during irradiation (Fig. 5b), validating the generation of $^{\bullet}O_2^-$. Electrochemical analysis on a rotating disk electrode (RDE) was conducted to determine the average electron-transfer number. Linear sweep voltammetry (LSV) curves of Bi-TCPP-NPs in O_2-saturated 0.1 M phosphate buffer solution (pH = 7) were recorded at different rotations to investigate the mechanism (Fig. 5c). Based on Koutecky–Levich plots at −0.80 V *vs.* Ag/AgCl, the average electron transfer number for Bi-TCPP-NPs involved in the ORR process was determined to be 2, which is consistent with the proposed photocatalytic process. In the WOR half-reaction, the production of H_2O_2 (147.19 μM) showed minimal variation when IPA was introduced to quench hydroxyl radicals. Additionally, DMPO-$^{\bullet}OH$ signals were absent in the ESR spectral measurements under illumination (Fig. 5b), suggesting that hydroxyl radicals do not participate in the water oxidation process. Ar bubbling to remove O_2 and $NaIO_3$ added as an electron acceptor confirmed the photochemical generation of O_2 from water *via* a four-electron pathway ($2H_2O + 4h^+ \rightarrow O_2 + 4H^+$). Based on these experiments and analysis, a plausible mechanism is proposed for Bi-TCPP-NPs' photocatalytic H_2O_2 production (Fig. 5d). Under visible light excitation, electron–hole pairs are separated. Low-coordinated Bi centers facilitate H_2O adsorption and act as sites for the WOR, thereby generating O_2 and supplying H^+. The electron-rich porphyrin group serves as the active center for the ORR to produce H_2O_2 through a two-step single-electron ORR process.

Conclusions

In summary, a novel non-centrosymmetric structure, Bi-TCPP, was constructed by asymmetrically arranging achiral porphyrin ligands on a 2D grid-like network. Notably, the formation of Bi-TCPP is accompanied by spiral crystal growth, resulting in an asymmetric morphology. This work provides a perspective to understand supramolecular chiral stacking using porphyrin-based achiral molecules. Moreover, this investigation paves new pathways for the enhancement of MOF functional properties by manipulating their morphology through a modulator-assisted strategy.

Author contributions

L. He carried out the experimental work and wrote the manuscript. E. Chen, J. Zhang and Q. Lin supervised the study and reviewed the manuscript. J. Xiang and Y. Guo helped with the characterization studies. All the authors discussed the results and contributed to the manuscript.

Data availability

The data supporting this article have been included as part of the ESI.† Crystallographic data for TCPP-Bi have been deposited at the CCDC under 2294422.†

Conflicts of interest

There are no conflicts to declare.

Acknowledgements

This work was financially supported by the National Natural Science Foundation of China (22201283), the National Science Foundation of Fujian Province (2022J05090 and 2022T3008), the Self-deployment Project Research Program of Haixi Institutes, Chinese Academy of Sciences (CXZX-2022-GH03), the Fujian Science & Technology Innovation Laboratory for Optoelectronic Information of China (2021ZR138), and the Open Project Program of the State Key Laboratory of Photocatalysis on Energy and Environment (SKLPEE-KF202204).

References

1 (*a*) C. Zhang, Z.-P. Yan, X.-Y. Dong, Z. Han, S. Li, T. Fu, Y.-Y. Zhu, Y.-X. Zheng, Y.-Y. Niu and S.-Q. Zang, Enantiomeric MOF Crystals Using Helical Channels as Palettes with Bright White Circularly Polarized Luminescence, *Adv. Mater.*, 2020, **32**, 2002914; (*b*) J.-H. Huang, Z.-Y. Wang, S.-Q. Zang and T. C. W. Mak, Spontaneous Resolution of Chiral Multi-Thiolate-Protected Ag_{30} Nanoclusters, *ACS Cent. Sci.*, 2020, **6**, 1971; (*c*) D. Niu, Y. Jiang, L. Ji, G. Ouyang and M. Liu, Self-Assembly through Coordination and π-Stacking: Controlled Switching of Circularly Polarized Luminescence, *Angew. Chem., Int. Ed.*, 2019, **58**, 5946.

2 X. Dou, N. Mehwish, C. Zhao, J. Liu, C. Xing and C. L. Feng, Supramolecular Hydrogels with Tunable Chirality for Promising Biomedical Applications, *Acc. Chem. Res.*, 2020, **53**, 852.

3 J. Zhang, S. Chen, T. Wu, P. Feng and X. Bu, Homochiral Crystallization of Microporous Framework Materials from Achiral Precursors by Chiral Catalysis, *J. Am. Chem. Soc.*, 2008, **130**, 12882.

4 (*a*) Y. Lu, H. Zhang, J. Y. Chan, R. Ou, H. Zhu, M. Forsyth, E. M. Marijanovic, C. M. Doherty, P. J. Marriott, M. M. B. Holl and H. Wang, Homochiral MOF-Polymer Mixed Matrix Membranes for Efficient Separation of Chiral Molecules, *Angew. Chem., Int. Ed.*, 2019, **58**, 16928; (*b*) X. Zhao, M. Wong, C. Mao, T. X. Trieu, J. Zhang, P. Feng and X. Bu, Size-Selective Crystallization of Homochiral Camphorate Metal-Organic Frameworks for Lanthanide Separation, *J. Am. Chem. Soc.*, 2014, **136**, 12572.

5 (*a*) S. Huang, H. Yu and Q. Li, Supramolecular Chirality Transfer toward Chiral Aggregation: Asymmetric Hierarchical Self-Assembly, *Adv. Sci.*, 2021, **8**, 2002132; (*b*) M. Liu, L. Zhang and T. Wang, Supramolecular Chirality in Self-Assembled Systems, *Chem. Rev.*, 2015, **115**, 7304.

6 (*a*) M. Wehner and F. Würthner, Supramolecular polymerization through kinetic pathway control and living chain

growth, *Nat. Rev. Chem.*, 2020, **4**, 38; (*b*) Y. Li, C. Liu, X. Bai, F. Tian, G. Hu and J. Sun, Enantiomorphic Microvortex-Enabled Supramolecular Sensing of Racemic Amino Acids by Using Achiral Building Blocks, *Angew. Chem., Int. Ed.*, 2020, **59**, 3486.

7 J. M. Ribó, J. Crusats, F. Sagués, J. Claret and R. Rubires, Chiral Sign Induction by Vortices During the Formation of Mesophases in Stirred Solutions, *Science*, 2001, **292**, 2063.

8 L. Zhang, T. Wang, J. Jiang and M. Liu, Chiral porphyrin assemblies, *Aggregate*, 2023, **4**, e198.

9 L. He, Y.-J. Guo, Y.-H. Xiao, E.-X. Chen, M.-B. Luo, Z.-H. Li and Q. Lin, Imparting Superhydrophobicity to Porphyrinic Coordination Frameworks Using Organotin, *CCS Chem.*, 2021, **4**, 2286.

10 (*a*) I. Goldberg, Crystal engineering of nanoporous architectures and chiral porphyrin assemblies, *CrystEngComm*, 2008, **10**, 637; (*b*) J.-W. Wang, L.-Z. Qiao, H.-D. Nie, H.-H. Huang, Y. Li, S. Yao, M. Liu, Z.-M. Zhang, Z.-H. Kang and T.-B. Lu, Facile electron delivery from graphene template to ultrathin metal-organic layers for boosting CO_2 photoreduction, *Nat. Commun.*, 2021, **12**, 813.

11 M. J. Van Vleet, T. Weng, X. Li and J. R. Schmidt, In Situ, Time-Resolved, and Mechanistic Studies of Metal–Organic Framework Nucleation and Growth, *Chem. Rev.*, 2018, **118**, 3681.

12 J. Duan, Y. Li, Y. Pan, N. Behera and W. Jin, Metal-organic framework nanosheets: An emerging family of multifunctional 2D materials, *Coord. Chem. Rev.*, 2019, **395**, 25.

13 A. Ben-Moshe, A. da Silva, A. Müller, A. Abu-Odeh, P. Harrison, J. Waelder, F. Niroui, C. Ophus, A. M. Minor, M. Asta, W. Theis, P. Ercius and A. P. Alivisatos, The chain of chirality transfer in tellurium nanocrystals, *Science*, 2021, **372**, 729.

14 (*a*) M. Shoaee, M. W. Anderson and M. P. Attfield, Crystal Growth of the Nanoporous Metal-Organic Framework HKUST-1 Revealed by In Situ Atomic Force Microscopy, *Angew. Chem., Int. Ed.*, 2008, **47**, 8525; (*b*) P. Y. Moh, P. Cubillas, M. W. Anderson and M. P. Attfield, Revelation of the Molecular Assembly of the Nanoporous Metal Organic Framework ZIF-8, *J. Am. Chem. Soc.*, 2011, **133**, 13304; (*c*) P. Cubillas, M. W. Anderson and M. P. Attfield, Crystal Growth Mechanisms and Morphological Control of the Prototypical Metal-Organic Framework MOF-5 Revealed by Atomic Force Microscopy, *Chem. – Eur. J.*, 2012, **18**, 15406.

15 (*a*) M. C. di Gregorio, L. J. W. Shimon, V. Brumfeld, L. Houben, M. Lahav and M. E. van der Boom, Emergence of chirality and structural complexity in single crystals at the molecular and morphological levels, *Nat. Commun.*, 2020, **11**, 380; (*b*) A. G. Shtukenberg, R. Drori, E. V. Sturm, N. Vidavsky, A. Haddad, J. Zheng, L. A. Estroff, H. Weissman, S. G. Wolf, E. Shimoni, C. Li, N. Fellah, E. Efrati and B. Kahr, Crystals of Benzamide, the First Polymorphous Molecular Compound, Are Helicoidal, *Angew. Chem., Int. Ed.*, 2020, **59**, 14593; (*c*) Q. Wen, S. Tenenholtz, L. J. W. Shimon, O. Bar-Elli, L. M. Beck, L. Houben, S. R. Cohen, Y. Feldman, D. Oron, M. Lahav and M. E. van der Boom, Chiral and SHG-Active Metal-Organic Frameworks Formed in Solution and on Surfaces: Uniformity, Morphology Control, Oriented Growth, and Postassembly Functionalization, *J. Am. Chem. Soc.*, 2020, **142**, 14210.

16 E. S. Grape, J. G. Flores, T. Hidalgo, E. Martínez-Ahumada, A. Gutiérrez-Alejandre, A. Hautier, D. R. Williams, M. O'Keeffe, L. Öhrström, T. Willhammar, P. Horcajada, I. A. Ibarra and A. K. Inge, A Robust and Biocompatible Bismuth Ellagate MOF Synthesized Under Green Ambient Conditions, *J. Am. Chem. Soc.*, 2020, **142**, 16795.

17 (*a*) F. M. Amombo Noa, E. Svensson Grape, S. M. Brülls, O. Cheung, P. Malmberg, A. K. Inge, C. J. McKenzie, J. Mårtensson and L. Öhrström, Metal–Organic Frameworks with Hexakis(4-carboxyphenyl)benzene: Extensions to Reticular Chemistry and Introducing Foldable Nets, *J. Am. Chem. Soc.*, 2020, **142**, 9471; (*b*) A. K. Inge, M. Köppen, J. Su, M. Feyand, H. Xu, X. Zou, M. O'Keeffe and N. Stock, Unprecedented Topological Complexity in a Metal-Organic Framework Constructed from Simple Building Units, *J. Am. Chem. Soc.*, 2016, **138**, 1970; (*c*) M. Feyand, E. Mugnaioli, F. Vermoortele, B. Bueken, J. M. Dieterich, T. Reimer, U. Kolb, D. de Vos and N. Stock, Automated Diffraction Tomography for the Structure Elucidation of Twinned, Sub-micrometer Crystals of a Highly Porous, Catalytically Active Bismuth Metal–Organic Framework, *Angew. Chem., Int. Ed.*, 2012, **51**, 10373.

18 D. Xie, S. Wang, S. Li, W. Yang and Y.-S. Feng, A two-dimensional Bi-based porphyrin metal-organic framework photocatalyst for white light-driven selective oxidation of sulfides, *Catal. Sci. Technol.*, 2022, **12**, 3254.

19 (*a*) F. Meng, S. A. Morin, A. Forticaux and S. Jin, Screw Dislocation Driven Growth of Nanomaterials, *Acc. Chem. Res.*, 2013, **46**, 1616; (*b*) A. G. Shtukenberg, Y. O. Punin, A. Gujral and B. Kahr, Growth Actuated Bending and Twisting of Single Crystals, *Angew. Chem., Int. Ed.*, 2014, **53**, 672.

20 (*a*) X. Liu, Z. Shi, M. Xie, J. Xu, Z. Zhou, S. Jung, G. Cui, Y. Zuo, T. Li, C. Yu, Z. Liu and S. Zhang, Single-Handed Double Helix and Spiral Platelet Formed by Racemate of Dissymmetric Cages, *Angew. Chem., Int. Ed.*, 2021, **60**, 15080; (*b*) A. G. Shtukenberg, Z. Zhu, Z. An, M. Bhandari, P. Song, B. Kahr and M. D. Ward, Illusory spirals and loops in crystal growth, *Proc. Natl. Acad. Sci. U. S. A.*, 2013, **110**, 17195; (*c*) S. A. Morin, A. Forticaux, M. J. Bierman and S. Jin, Screw Dislocation-Driven Growth of Two-Dimensional Nanoplates, *Nano Lett.*, 2011, **11**, 4449.

21 (*a*) A. Ohira, K. Okoshi, M. Fujiki, M. Kunitake, M. Naito and T. Hagihara, Versatile Helical Polymer Films: Chiroptical Inversion Switching and Memory with Re-Writable (RW) and Write-Once Read-Many (WORM) Modes, *Adv. Mater.*, 2004, **16**, 1645; (*b*) A. Tsuda, M. A. Alam, T. Harada, T. Yamaguchi, N. Ishii and T. Aida, Spectroscopic Visualization of Vortex Flows Using Dye-

Containing Nanofibers, *Angew. Chem., Int. Ed.*, 2007, **46**, 8198; (*c*) P. Yao, H. Wang, P. Chen, X. Zhan, X. Kuang, D. Zhu and M. Liu, Hierarchical Assembly of an Achiral π-Conjugated Molecule into a Chiral Nanotube through the Air/Water Interface, *Langmuir*, 2009, **25**, 6633; (*d*) Y. Qiu, P. Chen and M. Liu, Evolution of Various Porphyrin Nanostructures via an Oil/Aqueous Medium: Controlled Self-Assembly, Further Organization, and Supramolecular Chirality, *J. Am. Chem. Soc.*, 2010, **132**, 9644.

22 (*a*) Y. Kondo, Y. Kuwahara, K. Mori and H. Yamashita, Design of metal-organic framework catalysts for photocatalytic hydrogen peroxide production, *Chem*, 2022, **8**, 2924; (*b*) J. Zhang, H. Lei, Z. Li, F. Jiang, L. Chen and M. Hong, Halogen-Modulated 2D Coordination Polymers for Efficient Hydrogen Peroxide Photosynthesis under Air and Pure Water Conditions, *Angew. Chem., Int. Ed.*, 2024, **63**, e202316998; (*c*) J. Y. Choi, B. Check, X. Fang, S. Blum, H. T. B. Pham, K. Tayman and J. Park, Photocatalytic Hydrogen Peroxide Production through Functionalized Semiconductive Metal–Organic Frameworks, *J. Am. Chem. Soc.*, 2024, **146**, 11319; (*d*) Y. Zheng, H. Zhou, B. Zhou, J. Mao and Y. Zhao, Photocatalytic production of H_2O_2 over facet-dependent Ti-MOF, *Catal. Sci. Technol.*, 2022, **12**, 969.

23 (*a*) J. Wang, Y. Gong, M. Gao, Y. Zheng, Y. Feng, M. Xu, Q. Chu and J. Yan, $Bi_2O_2CO_3$ Nanosheet Composites with Bi-Based Metal–Organic Frameworks for Photocatalytic H_2O_2 Production, *ACS Appl. Nano Mater.*, 2024, **7**, 1067; (*b*) Y. Kofuji, Y. Isobe, Y. Shiraishi, H. Sakamoto, S. Tanaka, S. Ichikawa and T. Hirai, Carbon Nitride–Aromatic Diimide–Graphene Nanohybrids: Metal-Free Photocatalysts for Solar-to-Hydrogen Peroxide Energy Conversion with 0.2% Efficiency, *J. Am. Chem. Soc.*, 2016, **138**, 10019; (*c*) Y. Kofuji, S. Ohkita, Y. Shiraishi, H. Sakamoto, S. Tanaka, S. Ichikawa and T. Hirai, Graphitic Carbon Nitride Doped with Biphenyl Diimide: Efficient Photocatalyst for Hydrogen Peroxide Production from Water and Molecular Oxygen by Sunlight, *ACS Catal.*, 2016, **6**, 7021; (*d*) Y. Shiraishi, S. Kanazawa, Y. Kofuji, H. Sakamoto, S. Ichikawa, S. Tanaka and T. Hirai, Sunlight-Driven Hydrogen Peroxide Production from Water and Molecular Oxygen by Metal-Free Photocatalysts, *Angew. Chem., Int. Ed.*, 2014, **53**, 13454.

24 (*a*) Q. Liao, Q. Sun, H. Xu, Y. Wang, Y. Xu, Z. Li, J. Hu, D. Wang, H. Li and K. Xi, Regulating Relative Nitrogen Locations of Diazine Functionalized Covalent Organic Frameworks for Overall H_2O_2 Photosynthesis, *Angew. Chem., Int. Ed.*, 2023, **62**, e202310556; (*b*) M. Kou, Y. Wang, Y. Xu, L. Ye, Y. Huang, B. Jia, H. Li, J. Ren, Y. Deng, J. Chen, Y. Zhou, K. Lei, L. Wang, W. Liu, H. Huang and T. Ma, Molecularly Engineered Covalent Organic Frameworks for Hydrogen Peroxide Photosynthesis, *Angew. Chem., Int. Ed.*, 2022, **61**, e202200413; (*c*) S. Chai, X. Chen, X. Zhang, Y. Fang, R. S. Sprick and X. Chen, Rational design of covalent organic frameworks for efficient photocatalytic hydrogen peroxide production, *Environ. Sci.: Nano*, 2022, **9**, 2464.